https://doi.org/10.1016/j.engstruct.2023.116423

Experimental investigation on the structural performance of the high-strength ring strengthened dowel connection under monotonic load

Jiachen GUO[1], Tak-Ming CHAN[1,*], Yuhong WANG[1]

Department of Civil and Environmental Engineering, The Hong Kong Polytechnic University, Hong Kong, China

* Corresponding author: tak-ming.chan@polyu.edu.hk

Abstract

Traditional dowel connections embedded into concrete are susceptible to localised concrete crushing under heavy wheel loads. To address this issue, this paper introduces an innovative high-strength ring strengthened dowel connection to improve the bearing resistance of concrete at the joint surface. Monotonic load tests were conducted to investigate the effects of the high-strength ring concrete compressive strength, the high-strength ring thickness and length on improving ultimate load and mitigating localised concrete crushing. Test results indicated that the ultimate load and the initial stiffness of the specimen were greatly improved after applying the high-strength rings. Because of the excellent compressive resistance of the ring concrete, the initiation of the crushing zone was delayed, and the maximum compressive stress in normal strength concrete was reduced with the increase of the ring thickness. In addition, the deflection response of the dowel connection embedded into concrete could be predicted by the beam on elastic foundation (BEF) and the beam on inelastic foundation (BIF) theories. Based on the deformation of the dowel connection and surrounding concrete, the analytical solution was derived to predict the ultimate load of the high-strength ring strengthened dowel connection embedded into concrete.

Keywords: high-strength ring strengthened dowel connection; compressive stress concentration; ultimate load; beam on elastic foundation (BEF); beam on inelastic foundation (BIF); analytical solution.

1. Introduction

As one of the main components of rural and urban infrastructure, highways and municipal road systems play a vital role in promoting economic development. Well-developed highway systems facilitate economic and social interactions between different metropolises, and local transportation networks ensure convenient travel activities and the fast transportation of commercial goods [1-3]. However, due to the rapid increase in traffic volume over the past two decades, most of existing road systems have suffered premature damages within service life, thereby requiring urgent maintenance and rehabilitation [3-6].

In terms of the widely applied jointed plain concrete pavement (JPCP) systems, the structural performance of these rigid pavements closely depends on the pavement joint design including contraction joint, expansion joint and construction joint. Among these joints, the contraction joint to mitigate the induced tensile stress is the most critical because concrete is an anisotropic material strong in compression while weak in tension. To improve the integrity of concrete pavements at joint locations, epoxy-coated steel dowel bars are always installed along transverse joints with a spacing of 300 mm [1, 3, 7-10]. The main role of discrete dowel bars is to achieve an effective load transfer between pavement slabs and the load transfer mechanism of the dowel bar embedded into concrete is introduced in Fig. 1(a) [11]. Because of the high vertical stiffness of concrete, the relative deflection between pavement slabs is minimised during load transfer.

However, as stressed in Fig. 1(b), high compressive stress is caused at the pavement joint surface under heavy wheel loads. This severe compressive stress concentration has been extensively analysed through experimental tests and finite element analysis (FEA) [12-20]. After millions of load repetitions, compressive stress concentration around dowel bars may induce localised concrete crushing, thereby deteriorating the pavement joint stiffness and leading to the reduction of load transfer efficiency [21-24].

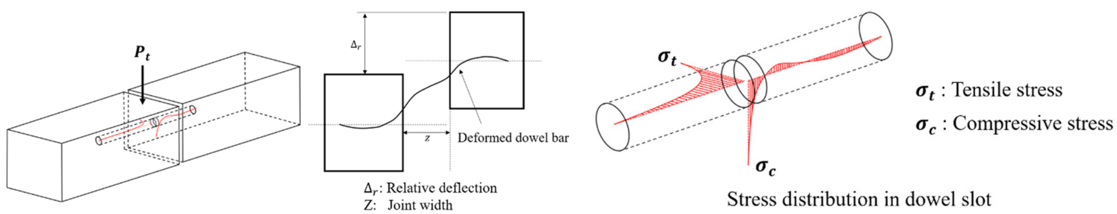

(a) (b)

Fig. 1. Load transfer mechanism of dowel bar embedded into concrete (a) load transfer mechanism, (b) stress distribution within dowel slot [11].

To reduce the compressive stress created at the joint surface, dowel bars have been updated with different shapes to increase the contact area between concrete and steel. Porter et al. [21, 25] experimentally studied elliptical-section dowel bars and test results indicated that, with a larger contact area in contrast to the circular dowel bar, the application of elliptical dowel bars effectively lowered the concrete bearing stress at the joint surface. Hu et al. [26] carried out cyclic load tests to compare elliptical, square as well as circular dowel bars. After applying 864,000 cycles of repeated loads, specimens equipped with elliptical dowel bars exhibited excellent performance in mitigating compressive stress concentration and the maximum bearing stress of concrete had been reduced by 40 percent [26]. Furthermore, plate dowel bars had also been proposed by American Concrete Pavement Association as shown in Fig. 2 [27]. These innovative diamond-plate as well as taper-plate dowel bars not only minimised the lock-in stress caused by the dowel bar misalignment, but also greatly expanded the contact surface between concrete and steel, thereby reducing the created contact stress.

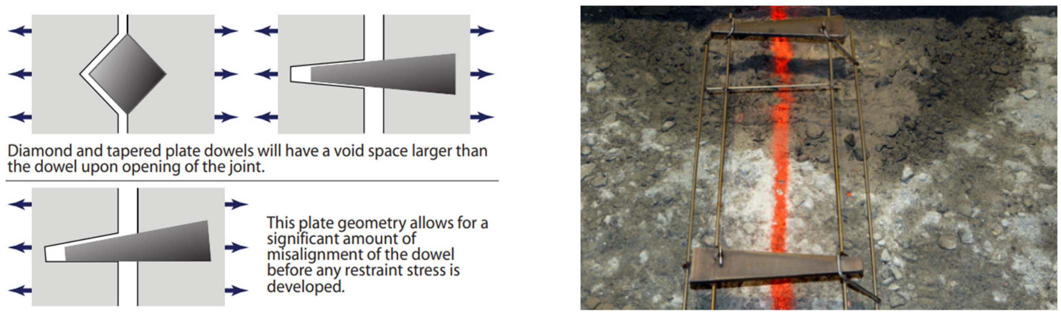

(a) (b)

Fig. 2. Diamond-shape and taper-shape dowel bars (a) configurations, (b) field application of taper-shape dowel bar [27].

However, although increasing the contact area between concrete and steel could mitigate compressive stress concentration, with the same section area, elliptical and plate dowel bars generally exhibit low flexural stiffnesses, which leads to large relative deflections between pavement slabs and thus impairs load transfer efficiency. Therefore, to mitigate localised concrete crushing failure, materials with excellent compressive behaviour are recommended in the fabrication of JPCP systems. One of these materials, ultra-high-performance concrete (UHPC), was initially proposed by De Larrard et al. [28] in France and has been developed for 30 years [29]. Normally, UHPC is produced with a low water-to-binder ratio, a high cementitious material content and fine mixtures, steel fibres and superplasticiser [30-35]. Because of the special mix design, in contrast to normal strength concrete (NSC), UHPC exhibits superior compressive strength, good toughness, high homogeneity and durability as well as low permeability [30, 36-41]. However, because of the large portion of cementitious materials involved, the fabrication of UHPC leads to a high material cost, which limits its widespread application [29, 42].

In this paper, an innovative high-strength ring strengthened dowel connection has been proposed and tested. As compressive stress concentration in JPCP systems primarily occurs at the pavement joint surface, high-strength rings made of concrete with excellent compressive resistance was applied to partially replace NSC. Fig. 3 shows the configuration of the concrete block with the high-strength ring strengthened dowel connections. Due to the small dimension of the ring part, the overall material cost of the high-strength ring strengthened dowel connection is not significantly increased.

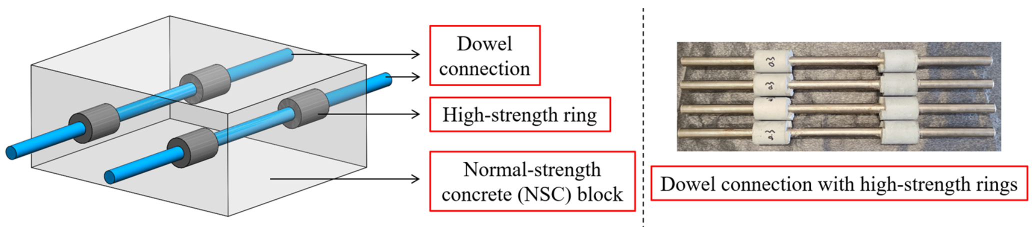

Fig. 3. High-strength ring strengthened dowel connection.

2. Experimental investigations

2.1. Materials

2.1.1. Concrete

In experimental tests, normal strength concrete (NSC) with the target cylinder compressive strength of 35 MPa was used to fabricate the concrete block. The corresponding mix proportions are presented in Table 1. Cylinder specimens were also prepared for each batch to evaluate the material properties of NSC on test days following BS EN 12390-3 [43] and BS EN 12390-6 [44]. Table 2 summarises the cylinder compressive strength and the splitting tensile strength measured at test days. As the thickness of the ring component was quite small, coarse aggregates were not included in the mix design to improve homogenity. As listed in Table 3, two types of concrete with water-to-binder ratios of 0.3 and 0.2, and target cylinder compressive strengths of 110 MPa and 140 MPa were adopted to fabricate high-strength rings. Effective superplasticiser was also used to minimise the amount of water usage and ensure excellent workability. Table 4 summarises material properties of the ring concrete measured prior to experimental tests. Uniaxial compressive stress-strain curves of NSC and the ring concrete are plotted in Fig. 4.

Table 1 Mix proportions of normal strength concrete (NSC) (kg/m^3).

ID	Water	Cement	Sand	Aggregate
NSC	210	420	620	1150

Table 2 Material properties of normal strength concrete.

ID	Compressive strength (MPa)	Splitting tensile strength (MPa)
NSC	34.45	3.59

Table 3 Ring concrete mix proportions (kg/m^3).

ID	Water	Cement	Silica fume	Sand (0.3-0.6 mm)	Sand (0.1-0.3 mm)	S.P.
Ring-0.3	340	1030	103	904	226	15
Ring-0.2	260	1040	260	832	208	30

S.P.: Superplasticiser

Table 4 Material properties of ring concrete.

ID	Compressive strength (MPa)	Splitting tensile strength (MPa)
Ring-0.3	117.3	6.38
Ring-0.2	145.3	7.20

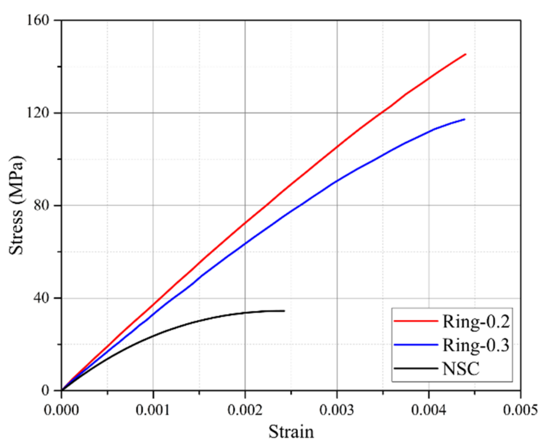

Fig. 4. Stress-strain relationships of normal strength concrete (NSC) and the ring concrete.

2.1.2. Steel dowel connection

The stress-strain relationship of the dowel connection was determined by carrying out uniaxial tensile tests. As shown in Fig. 5(a), with the application of the Instron 5982 electro-mechanical high force universal testing system, the modulus of elasticity of the dowel connection E_s was measured by attached strain gauges and the full-range stress-strain relationship was recorded by the video extensometer. Related material parameters of 16 mm and 19 mm dowel connections are tabulated in Table 5 and the corresponding stress-strain curves are depicted in Fig. 5(b).

Table 5 Material properties of dowel connections.

Dowel connection diameter	Modulus of elasticity E_s (GPa)	Yield strength $f_{y(0.2)}$ (MPa)	Ultimate strength f_u (MPa)	Elongation ε_f (%)
16 mm	211.9	490.4	577.7	14.4
19 mm	208.0	462.8	588.9	13.5

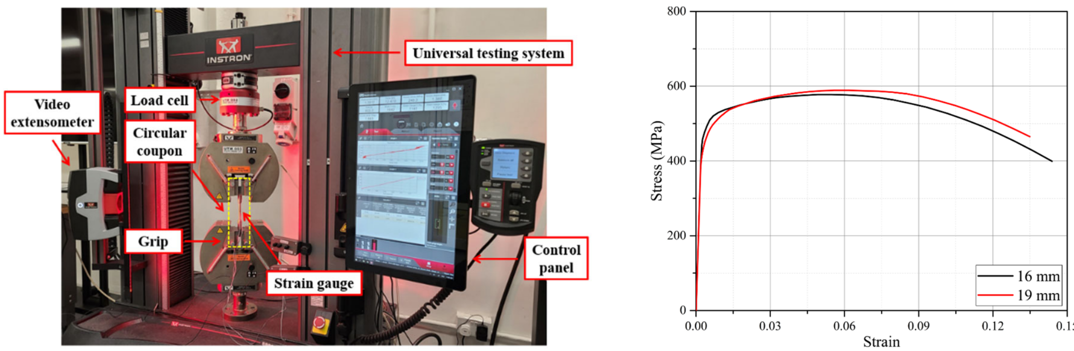

(a) (b)

Fig. 5. Uniaxial tensile tests of 16 mm and 19 mm dowel connections (a) test setup, (b) stress-strain curves.

2.2. Design of specimens

To investigate the effect of the high-strength ring on the ultimate load enhancement and the mitigation of localised concrete crushing, parameters including the cylinder compressive strength of the ring concrete, the thickness and the length of the high-strength ring were experimentally studied. The configuration and dimension of the test specimen are shown in Fig. 6. Two dowel connections with a length of 500 mm were installed in each concrete block to minimise the unexpected twisting under the vertical load. The spacing and the side distance of the dowel connection were 150 mm and 75 mm, respectively. To mitigate localised concrete crushing, four high-strength rings were placed at the joint surface, with the thickness (t) and length (l) of the ring part varying in different specimens. Regarding the diameter of the dowel connection (d), both 16 mm and 19 mm dowel connections were considered and compared. To improve the confidence of experimental test data, repeated tests were considered for specimens with different configurations. A total of 22 specimens were tested and each specimen was labelled by the dowel connection diameter, the ring thickness, the ring length and the water-to-binder ratio of the ring concrete in the subsequent analysis. For example, 16-10-50-0.2 represented that the specimen was equipped with 16 mm diameter dowel connections and high-strength rings that were 10 mm thick and 50 mm long, made of concrete with a water-to-binder ratio of 0.2.

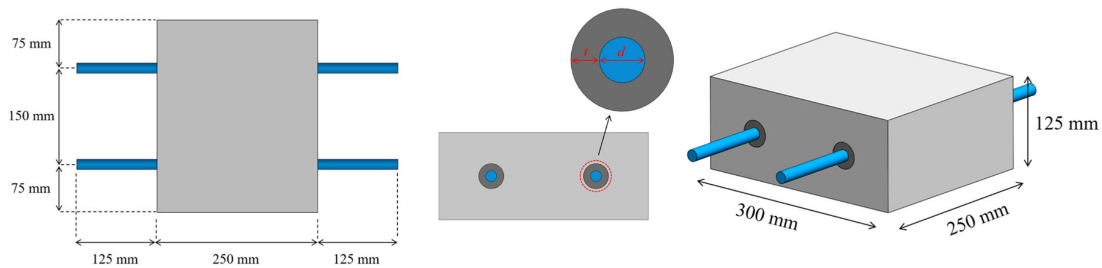

Fig. 6. Configuration and dimension of the test specimen.

2.3. Specimen preparation

As the test specimen consisted of the dowel connections, the high-strength rings and the NSC block, it was a challenge to complete the casting process at once. Therefore, in specimen preparation, high-strength rings were firstly casted on the dowel connection by using the designed acrylic formwork as shown in Fig. 7. The internal diameter of the acrylic tube was equal to the external diameter of the ring part. Before concrete casting, the high-strength ring casting device shown in Fig. 7(a) was fixed at the designed location of the dowel connection and placed on the flat platform as depicted in Fig. 7(b). Because of the effective superplasticiser, the excellent workability of the ring concrete was achieved, which promoted the casting process and ensured the homogeneity of the high-strength ring. Fig. 8 presents the hardened rings made of different types of ring concrete. Because of small w/b ratios, all ring parts were firstly cured in the moulds for three days to fully develop the early-stage autogenous shrinkage [45]. After that, as seen in Fig. 9(a), dowel connections with rings were demoulded and fixed in the acrylic formworks for the NSC block casting. The entire specimen after concrete hardening could be found in Fig. 9(b). As NSC block and the ring part experienced similar drying shrinkage in the first month [46], few cracks formed at the interface of these two components. After curing for 28 days, prepared specimens were tested under monotonic loads.

(a) (b)

Fig. 7. High-strength ring casting device (a) ring casting formwork, (d) ring casting platform.

(a) (b)

Fig. 8. Dowel connections with high-strength rings (a) water-to-binder ratio: 0.3, (b) water-to-binder ratio: 0.2.

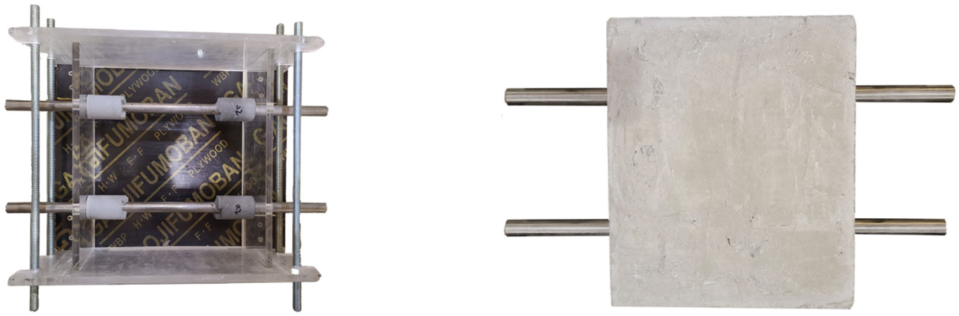

(a) (b)

Fig. 9. Concrete block casting (a) acrylic formwork with dowel connections and high-strength rings, (b) hardened concrete block with high-strength ring strengthened dowel connections.

2.4. Test setup and instrumentation

To investigate the load bearing capacity of the dowel connection embedded into concrete under vertical load, as depicted in Fig. 10, a support frame with the V-shape devices was fabricated and acted as a rigid seat to support the dowel connections. Fig. 11 shows the setup of the monotonic load test which was conducted through MTS 815 rock system. A 0.1 mm/min displacement-controlled vertical load was applied to the concrete block by two load blocks located at the joint surface. A load cell with a capacity of 300 kN was placed between the ball joint and the rigid plate to measure the applied load. The joint width between the concrete block and the V-shape support device was 10 mm. Regarding the test instrumentations, both linear variable differential transducers (LVDTs) and strain gauges were employed to monitor the deflection response and the strain development with the increased vertical load. A total of four LVDTs were placed at the corners of the support frame as shown in Fig. 12(a). The average of LVDT measurements was taken as the vertical deflection of the concrete block. In terms of the strain measurement, as the main role of the ring part was to relieve the localised concrete crushing in the NSC block, four strain gauges (SG1 to SG4) were attached on the top of dowel connections to monitor the compressive strain development of NSC as shown in Fig. 12(b). Due to the small thickness of the ring part, it was difficult to assess the strain development of the ring concrete by strain gauges.

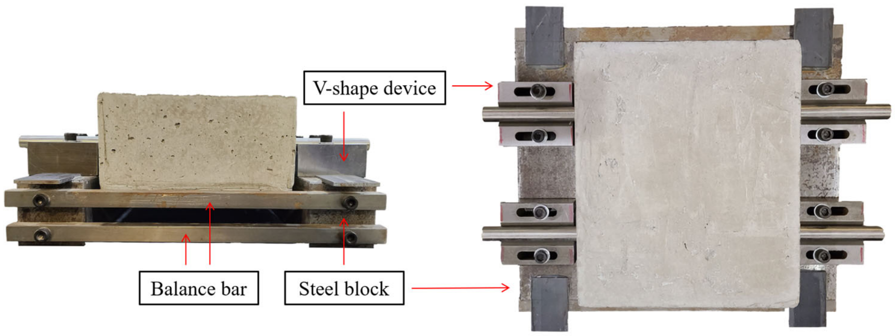

Fig. 10. Designed support frame.

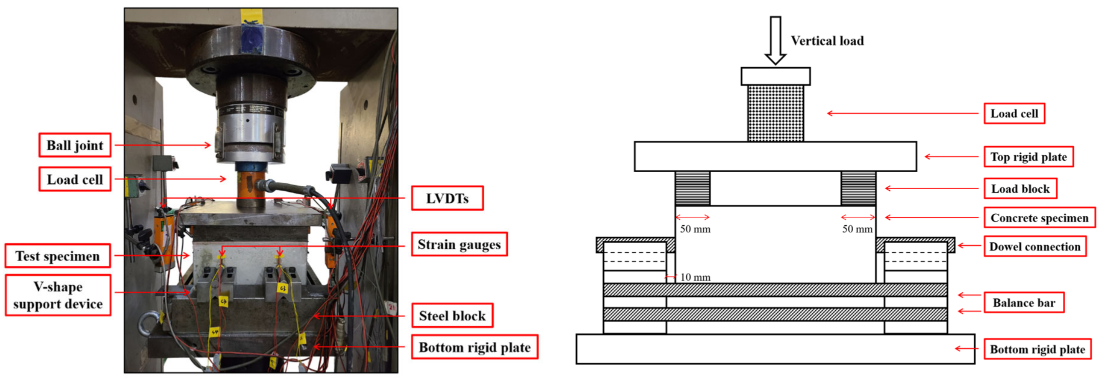

(a) (b)

Fig. 11. Experimental test setup (a) front view, (b) side view

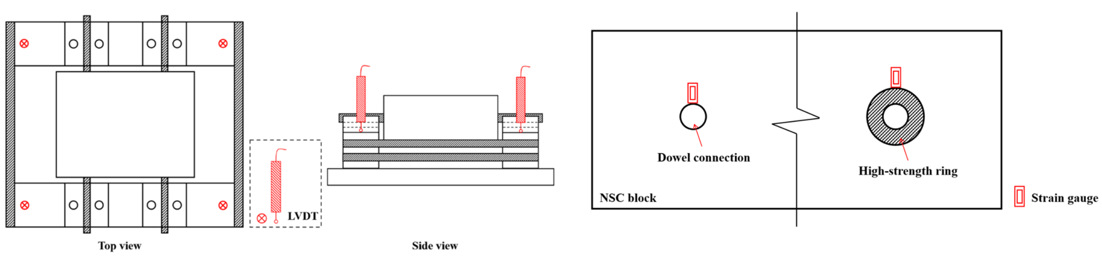

(a) (b)

Fig. 12. LVDTs and strain gauges arrangements (a) LVDTs arrangements, (b) positions of strain gauges.

3. Results and discussion

3.1. Failure modes

Under vertical load, the dowel connection at the joint surface was subjected to the transferred shear force and the moment induced by the support reaction force. In experimental tests, once the maximum compressive stress exceeded the compressive strength of concrete, localised concrete crushing started to initiate at the top of the dowel connection and propagated as the vertical load increased. Besides, because of the low tensile strength of concrete, horizontal concrete tensile cracks also formed around dowel connections and propagated horizontally. Fig. 13 shows the typical concrete crushing and horizontal tensile cracks which are highlighted by red lines and yellow lines, respectively. In contrast to specimens with traditional dowel connections, although concrete crushing failure was also observed in specimens with the high-strength rings, the higher compressive strength and crushing strain of the ring concrete considerably postponed the occurrence of the localised concrete crushing and improved the bearing resistance of the dowel connection. Furthermore, because of a large interface between NSC and the ring concrete, the compression zone of the NSC block was greatly expanded, which effectively mitigated the development of the localised concrete crushing as the vertical load increased. Similar observations were also found from the strain measurement that was discussed in section 3.3. Additionally, because of severe concrete crushing, the vertical load distribution among dowel connections became nonuniform after reaching ultimate load. As a result, due to the impaired shear resistance, brittle transverse shear cracks were possible to occur at regions suffering severe concrete crushing. Fig. 14 depicts transverse shear cracks created in different specimens. These shear cracks led to a sudden load drop at the end of experimental tests.

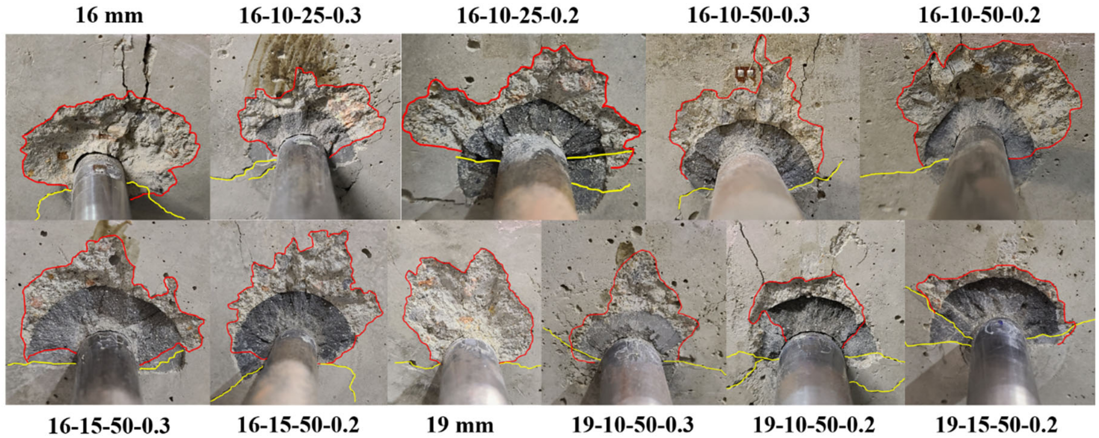

Fig. 13. Localised concrete crushing (red lines) and tensile cracks (yellow lines).

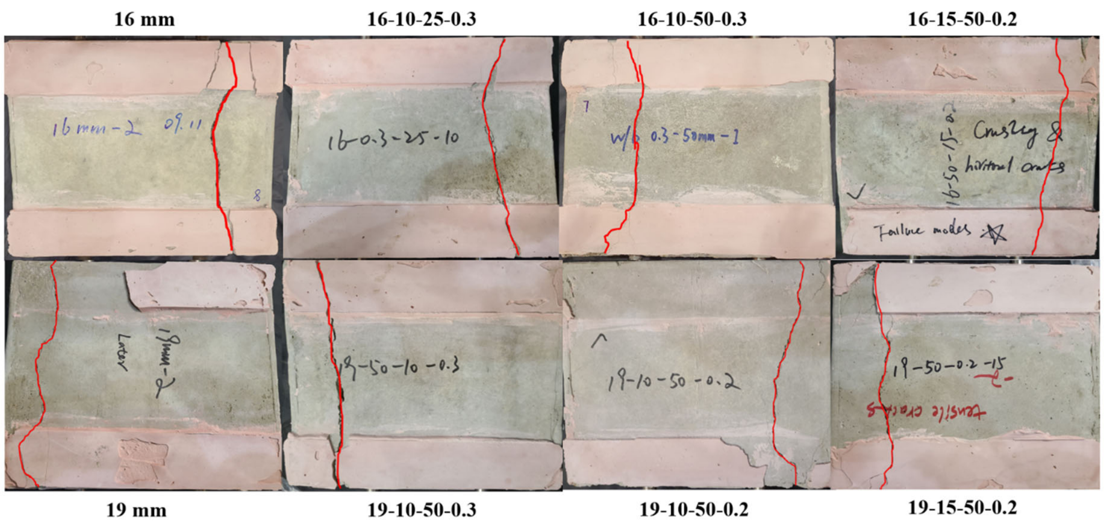

Fig. 14. Transverse shear cracks (red lines).

3.2. Deflection response

Load-deflection relationships of test specimens are plotted in Fig. 15, in which the full-range load-deflection curves could be divided into three stages: the elastic stage, the elasto-plastic stage and the plastic stage as indicated in Fig. 16. Within the elastic stage, the stiffness of the surrounding concrete was a constant and the deflection response of the dowel connection embedded into concrete remained elastic [47, 48]. After entering the elasto-plastic stage, as the vertical load increased, localised concrete crushing initiated at the joint surface and then propagated around the dowel connection. As a result, the support stiffness of surrounding concrete was deteriorated, thereby inducing a nonlinear deflection response. In the plastic stage, it started around the ultimate load, at which the localised crushing zone was fully expanded and the vertical load was nearly unchanged as the vertical deflection increased. However, as discussed in the failure mode section, unexpected transverse shear cracks might occur and result in a sudden load drop. Thus, the deflection response within the plastic stage was separated to two types based on different failure modes.

Table 6 and Table 7 summarise the initial stiffness k_{Δ} and the ultimate load N_u of each specimen, respectively. For specimens with the same configuration, the average stiffness $\overline{k_{\Delta}}$ and the average ultimate load $\overline{N_u}$ were employed. After incorporating high-strength rings with a 15 mm thickness, the ultimate loads of test specimens were increased by approximately 50 percent. Furthermore, specimens with high-strength rings exhibited higher initial stiffness in contrast to those with traditional dowel connections. This enhancement effect was more pronounced as the compressive strength and thickness of the ring component increased. However, because localised concrete crushing only occurred at the joint surface, the effects of the ring length on improving the ultimate load and the initial stiffness were not significant. Based on Fig. 15(a) and (b) and data collected in Table 6 and Table 7, specimens with high-strength rings of 25 mm length exhibited similar performance to those with 50 mm long rings in terms of the deflection response, the initial stiffness and the ultimate load.

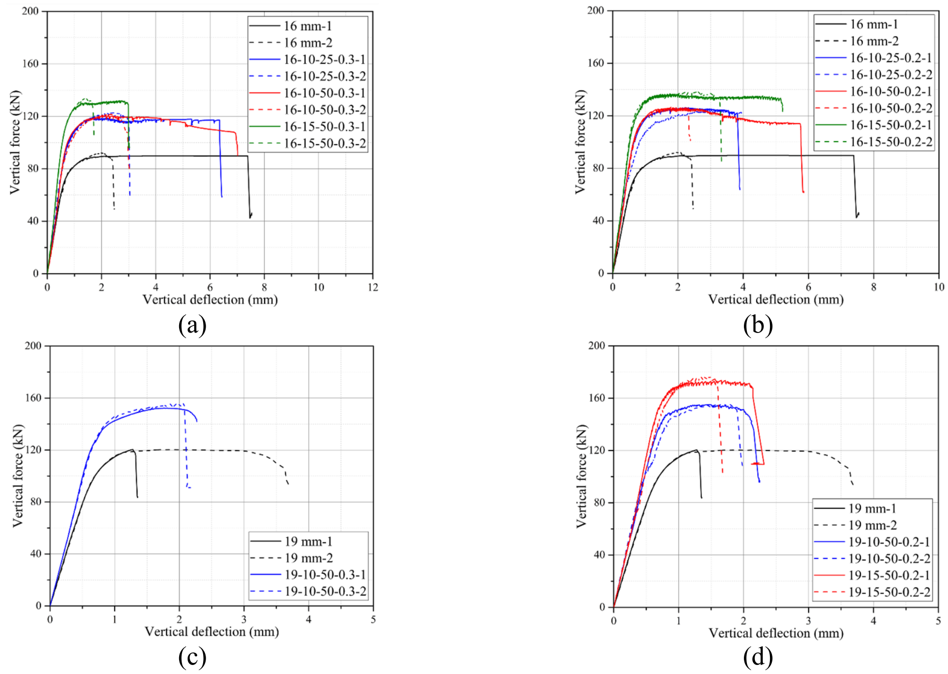

Fig. 15. Load-deflection relationships (a) 16-0.3, (b) 16-0.2, (c) 19-0.3, (d) 19-0.2.

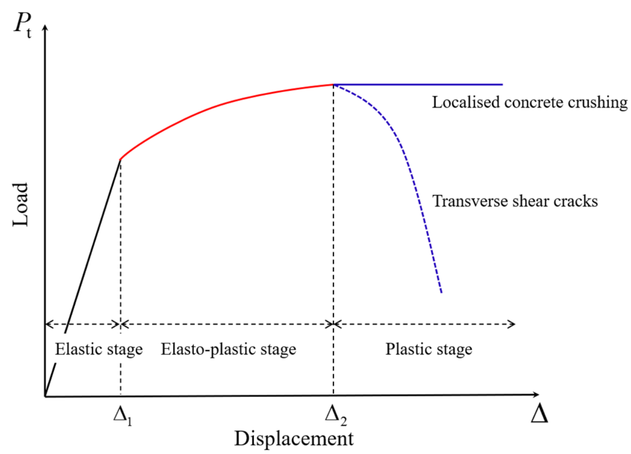

Fig. 16. Three-stage load deflection curve

Table 6 Summary of test results (16 mm dowel connection).

Specimen ID	k_Δ (kN/mm)	$\overline{k_\Delta}$ (kN/mm)	Stiffness ratio	N_u (kN)	$\overline{N_u}$ (kN)	Load ratio
16 mm-1	124.2	125.1	1	89.9	90.8	1
16 mm-2	126.0			91.6		
16-10-25-0.2-1	160.6	162.0	1.29	126.3	125.2	1.38
16-10-25-0.2-2	163.4			124.1		
16-10-25-0.3-1	143.3	146.0	1.17	119.4	121.1	1.33
16-10-25-0.3-2	148.7			122.7		
16-10-50-0.2-1	164.4	162.8	1.30	126.0	126.3	1.39
16-10-50-0.2-2	161.2			126.6		
16-10-50-0.3-1	142.1	143.2	1.14	120.6	121.0	1.33
16-10-50-0.3-2	144.3			121.4		
16-15-50-0.2-1	188.8	190.0	1.52	136.8	137.6	1.52
16-15-50-0.2-2	191.2			138.4		
16-15-50-0.3-1	178.7	176.8	1.41	132.0	133.3	1.47

16-15-50-0.3-2	174.9			134.5		

Table 7 Summary of test results (19 mm dowel connection).

Specimen ID	k_Δ (kN/mm)	$\overline{k_\Delta}$ (kN/mm)	Stiffness ratio	N_u (kN)	$\overline{N_u}$ (kN)	Load ratio
19 mm-1	152.9	156.0	1	120.4	120.3	1
19 mm-2	159.1			120.2		
19-10-50-0.2-1	210.5	206.4	1.32	155.1	155.5	1.29
19-10-50-0.2-2	202.3			155.9		
19-10-50-0.3-1	194.5	192.4	1.23	152.1	154.0	1.28
19-10-50-0.3-2	190.3			155.9		
19-15-50-0.2-1	215.7	218.0	1.40	173.6	175.1	1.46
19-15-50-0.2-2	220.3			176.6		

3.3. Strain development in normal strength concrete (NSC)

The compressive strain development in NSC was assessed through the strain data recorded in experimental tests. Fig. 12(b) describes the layout of strain gauges as introduced in the test instrumentation section. Since the compressive strength of the ring concrete was around 3-4 times that of NSC, it was recommended to adopt ring parts to carry the concentrated compressive stress at the joint surface and mitigate the localised concrete crushing of NSC. With the average strain data recorded by four strain gauges, Fig. 17 depicts the NSC compressive strain evolutions in specimens with rings of different thicknesses. It was noted that the application of high-strength rings effectively lowered the compressive strain development in the NSC block and this effect became more pronounced as the ring thickness increased. Fig. 18 demonstrates the effect of the ring length on the compressive strain development of NSC. As compressive stress concentrated at a localised zone near the joint surface, the length of the ring part had a limited effect on the compressive strain evolution. Additionally, as seen in Fig. 18 and Fig. 19, the effect of the compressive strength of the ring concrete on the NSC compressive strain development was limited and not as significant as the thickness of the ring part.

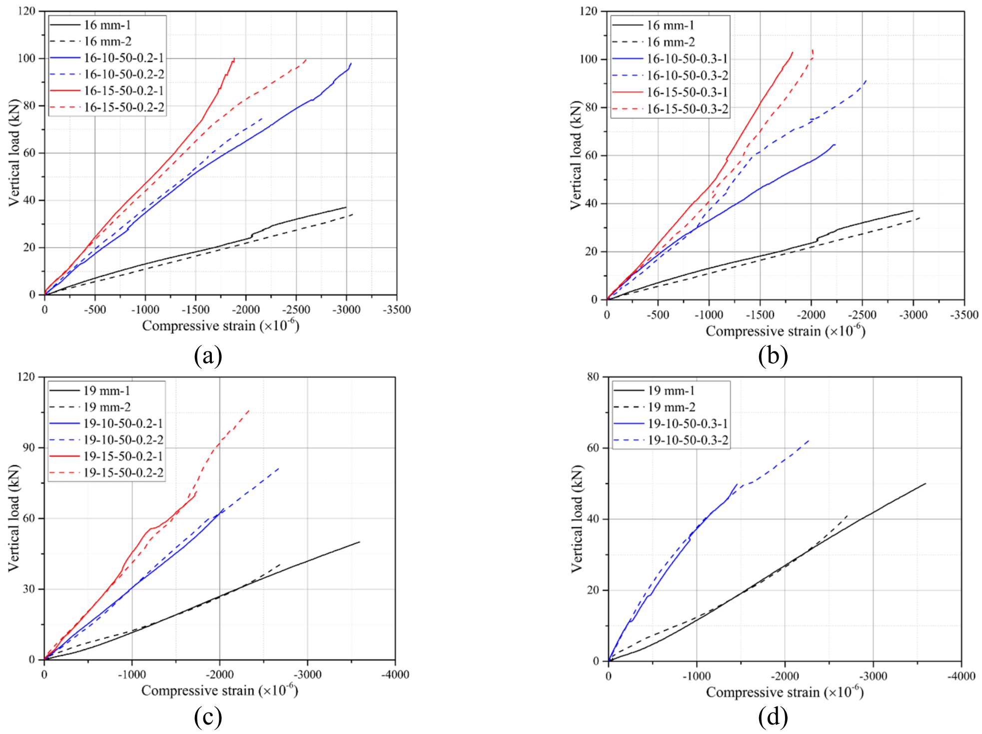

Fig. 17. NSC compressive strain evolution (a) 16 mm-0.2, (b) 16 mm-0.3, (c) 19 mm-0.2, (d) 19 mm-0.3.

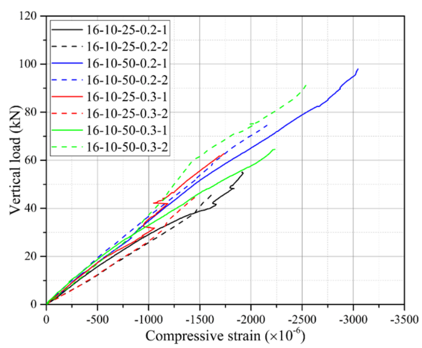

Fig. 18. NSC strain developments with different ring lengths.

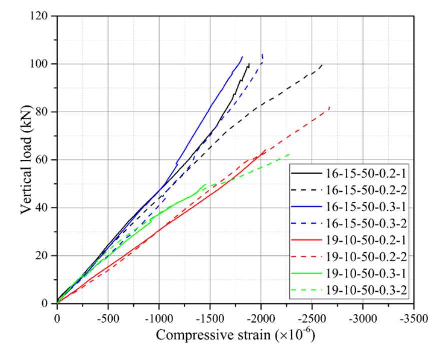

Fig. 19. NSC strain development with various ring concrete.

4. Prediction of deflection response

4.1. Beam on elastic foundation (BEF) theory

Within the elastic stage, the linear deflection response of the dowel connection embedded into concrete could be analysed through the beam on elastic foundation (BEF) theory [20, 48], in which the dowel connection was modelled by the infinite elastic beam and concrete was simulated by the Winkler foundation as shown in Fig. 20. Focusing on a single beam element, the differential equation of the BEF theory was derived as expressed by Eq. (1), where, x and y are the location and the vertical deformation of the beam element; k is the vertical stiffness of the elastic foundation modelled by discrete vertical springs; E and I refer to the modulus of elasticity and the moment of inertia of the dowel connection, respectively.

$$EI\frac{d^4y}{dx^4}+ky=0 \tag{1}$$

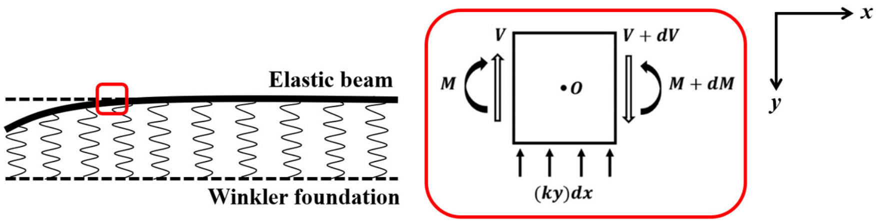

Fig. 20. Beam on elastic foundation (BEF) model.

The solution to Eq. (1) was generated as Eqs. (2) and (3), where A, B, C and D are constants determined by boundary conditions. When $x \to \infty$, the vertical deflection of the elastic beam was zero. As a result, A and B were both zero. Considering the test arrangement, as shown in Fig. 21, the vertical shear force V_0 and moment M_0 at the joint surface were determined as Eqs. (4) and (5), where P_t is the shear force taken by the individual dowel connection; z is the distance between the V-shape support device and the joint surface. Then the elastic deformation of the dowel connection embedded into concrete was derived as Eq. (6). When x = 0, the vertical deformation y_0 was calculated by Eq. (7).

$$y=e^{\beta x}\left(Acos\beta x+Bsin\beta x\right)+e^{-\beta x}\left(Ccos\beta x+Dsin\beta x\right) \tag{2}$$

$$\beta=\sqrt[4]{\frac{k}{4EI}} \tag{3}$$

$$V_0=\frac{dM}{dx}_{x=0}=-P_t \tag{4}$$

$$M_0 = -EI\frac{d^2 y}{dx^2}\bigg|_{x=0} = -P_t z \tag{5}$$

$$y = \frac{e^{-\beta x}}{2\beta^3 EI}\left[P_t cos\beta x + \beta P_t z\left(cos\beta x - sin\beta x\right)\right] \tag{6}$$

$$y_0 = \frac{P_t}{2\beta^3 EI}\left(1+\beta z\right) \tag{7}$$

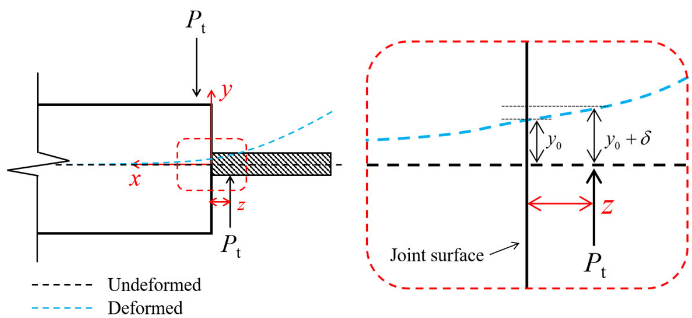

Fig. 21. Deflection analysis of the dowel connection embedded into concrete.

In experimental tests, the vertical deflection of the concrete block at the joint surface consisted of the dowel connection deformation y_0, the deflection caused by the slope of the dowel connection zdy_0/dx, the moment deflection $P_t z^3/12EI$ as well as the shear deflection $\frac{\lambda P_t}{AG}$, where λ is the shape factor equal to 10/9 for the circular section; A is the section area of the dowel bar; G is the shear modulus of the dowel connection. However, as the distance z and the slope of the dowel connection dy_0/dx were quite small, as depicted in Fig. 21, it was reasonable to neglect these two components and the vertical deflection at the joint surface Δ was simplified to Eq. (8).

$$\Delta = y_0 + \delta = P_t\left[\frac{\left(1+\beta z\right)}{2\beta^3 EI} + \frac{\lambda}{AG}\right] \tag{8}$$

Therefore, within the elastic stage, the vertical deflection Δ increased proportionally to the transferred load P_t, and the initial stiffness of the test specimen closely depended on the section and the mechanical properties of the dowel connection and the stiffness of support concrete.

4.2. Beam on inelastic foundation (BIF) theory

With the increase of the vertical force, concrete around the dowel connection gradually entered the plastic state, thereby resulting in the deterioration of the concrete support stiffness. To model the deflection response within the nonlinear elasto-plastic stage, the beam on inelastic foundation (BIF) theory was developed to account for the concrete support stiffness reduction [49-54]. Soroushian et al. [55] and Dei Poli et al. [56] claimed that the consistently damaged concrete support stiffness was closely related to the ratio of the vertical deflection to the dowel connection diameter. Based on this conclusion, Maekawa et al. [50] proposed a non-dimensional damage index *DI* to describe the consistent stiffness deterioration as expressed by Eqs. (9) to (11), where k refers to the elastic concrete support stiffness, d is the diameter of the dowel connection. The same *DI* was also adopted by Soltani et al. [49] and Moradi et al. [51] in the determination of the damaged support stiffness k_d.

$$k_{\mathrm{d}} = k \ (DI \leq 0.02) \tag{9}$$

$$k_{\mathrm{d}} = \frac{k}{\left[1+3(DI-0.02)^{0.8}\right]^{4}} \ (DI > 0.02) \tag{10}$$

$$DI = \frac{\Delta}{d} \tag{11}$$

However, Ma et al. [52] indicated that the displacement at the end of the elastic stage should be determined according to the deflection data since this value was sensitive to the test setup and the specimen configuration. Therefore, Eqs. (12) to (13) were proposed to model the damaged concrete support stiffness and the damage index *DI* was calculated by Eq. (11), where Δ_1 and Δ_2 are typical deflections at the initiation and the end of the elasto-plastic stage, respectively.

$$k_{\mathrm{d}} = k \ (\Delta \leq \Delta_1) \tag{12}$$

$$k_{\mathrm{d}} = \frac{k}{\left[1 + 3(DI - \frac{\Delta_1}{d})^{0.8}\right]^4} \quad (\Delta_1 < \Delta \le \Delta_2) \tag{13}$$

The deflection response of the high-strength ring strengthened dowel connection was derived according to the BEF and the BIF theories. As unexpected shear cracks might occur in experimental tests within the post-peak stage and lead to a sudden load drop, the deflection response prediction ended at the displacement when the ultimate load almost reached. The detailed calculation procedures are introduced in Fig. 22 and explained below.

1. Based on the deflection data recorded in experimental tests, the initial stiffness of the load deflection curve k_Δ was firstly determined through linear regression analysis. Then the typical deflection Δ_1 was defined at the end of the elastic stage.
2. Through Eq. (8), the relative stiffness of the dowel support β was calculated and then the concrete support stiffness k can be further obtained by Eq. (3).
3. After entering the elasto-plastic stage, the damaged concrete support stiffness k_{d} was computed with the damage index DI.
4. The damaged stiffness of the load-deflection curve $k_{\Delta,\mathrm{d}}$ was calculated with the damaged concrete support stiffness k_{d}.
5. The vertical load increment dP_{t} was then acquired by the deflection increment $d\Delta$ and the damaged stiffness $k_{\Delta,\mathrm{d}}$ of the load-deflection curve.

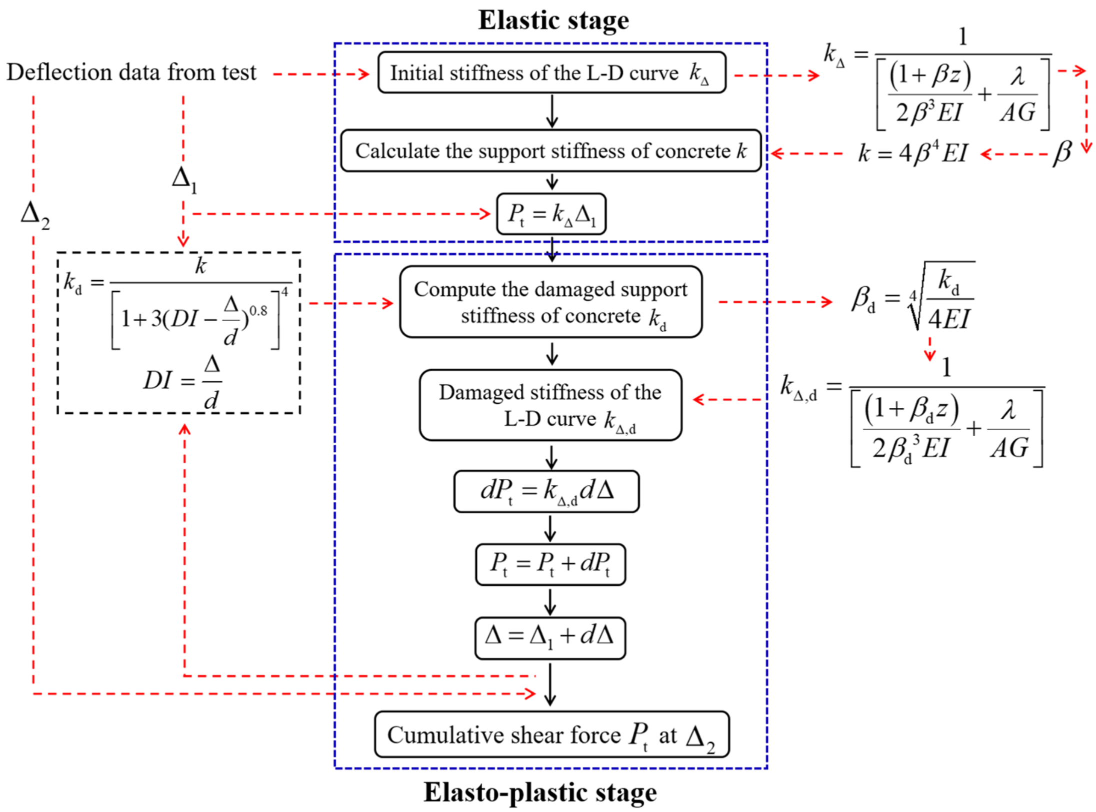

Fig. 22. The deflection response derivation based on BEF and BIF theories.

The vertical force increments were then summed to compute the total force at the end of the elasto-plastic stage, at which the corresponding deflection was Δ_2 and the ultimate load of the specimen remained almost constant with an increased deflection. Based on the deflection response derivation procedures, Fig. 23 plots the load-deflection curves predicted by the damage indices proposed by Moradi et al. [51] and Ma et al. [52], respectively. Table 8 summarises typical deflections and predicted ultimate loads. It was found that the ultimate loads were significantly overestimated by the models proposed by Moradi et al. [51] and Ma et al. [52], and the overestimation was possibly attributed to the underestimation of the concrete support stiffness deterioration. To capture the real deflection response, the stiffness reduction recommended by Ma et al. [52] had been updated as expressed by Eq. (14). The exponential coefficient 0.8 was changed to 0.35 to accelerate the stiffness reduction with the increase of the vertical deflection. After modification, as shown by red lines in Fig. 23 and data summarised in Table 8, the generated load-deflection curves and the predicted ultimate loads showed close matches to those recorded in experimental tests.

$$k_{\mathrm{d}} = \frac{k}{\left[1+3(DI-\dfrac{\Delta_1}{d})^{0.35}\right]^4} \quad (\Delta_1 < \Delta \le \Delta_2) \tag{14}$$

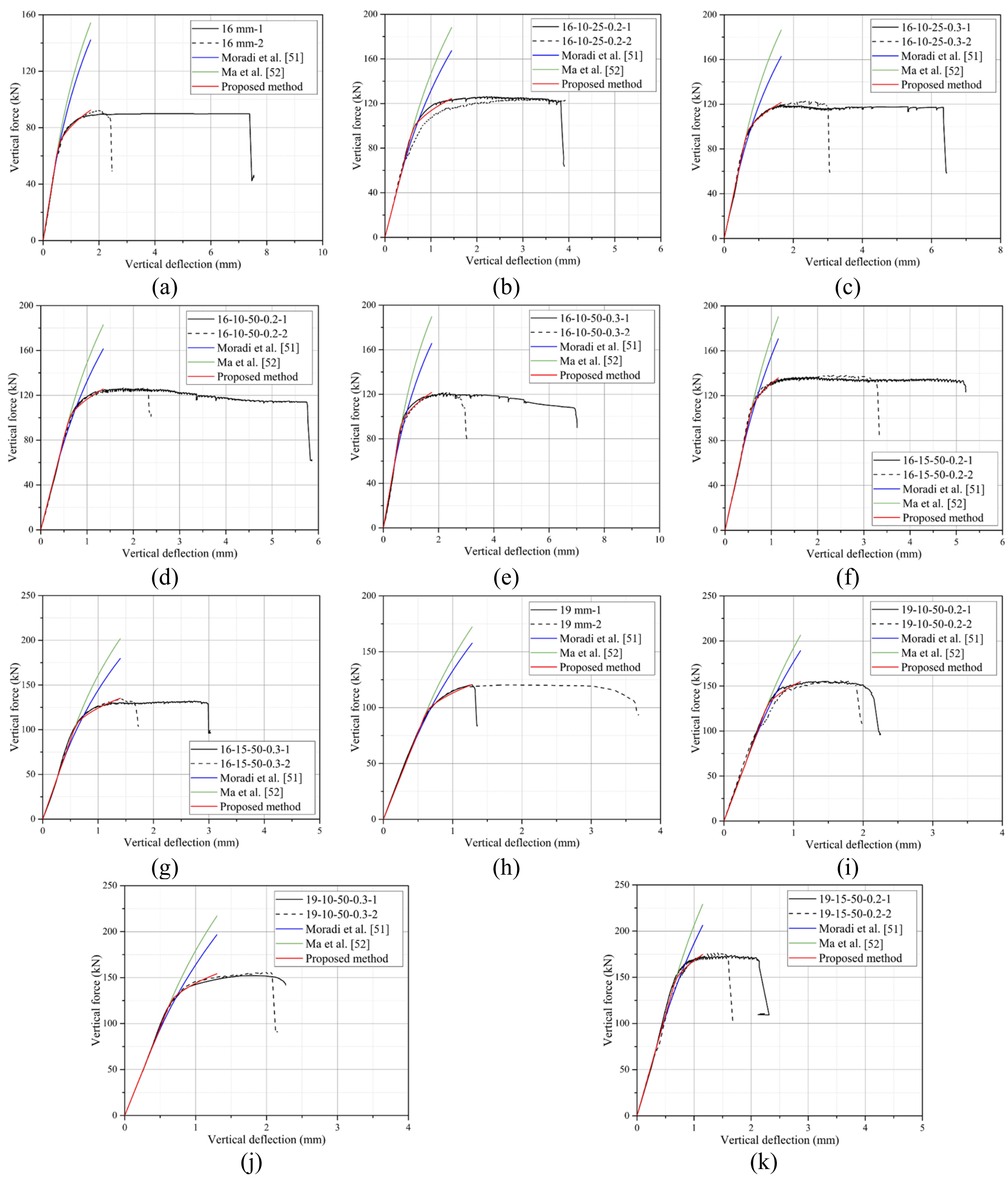

Fig. 23. Predicted load-deflection relationships (a) 16 mm, (b) 16-10-25-0.2, (c) 16-10-25-0.3, (d) 16-

10-50-0.2, (e) 16-10-50-0.3, (f) 16-15-50-0.2, (g) 16-15-50-0.3, (h) 19 mm, (i) 19-10-50-0.2, (j) 19-10-50-0.3, (k) 19-15-50-0.2.

Table 8 Predicted ultimate load with damaged concrete support stiffness.

Specimen ID	N_u (kN)	Δ_1 (mm)	Δ_2 (mm)	$N_{u,Moradi}$ (kN)	$\frac{N_{u,Moradi}}{N_u}$	$N_{u,Ma}$ (kN)	$\frac{N_{u,Ma}}{N_u}$	$N_{u,Pred}$ (kN)	$\frac{N_{u,Pred}}{N_u}$
16 mm-1	89.9	0.48	1.70	142.20	1.58	154.27	1.72	92.4	1.03
16 mm-2	91.6			142.20	1.55	154.27	1.68	92.4	1.01
16-10-25-0.2-1	126.3	0.56	1.45	167.39	1.33	188.11	1.49	124.57	0.99
16-10-25-0.2-2	124.1			167.39	1.35	188.11	1.52	124.57	1.00
16-10-25-0.3-1	119.4	0.5	1.65	162.83	1.36	186.38	1.56	121.59	1.02
16-10-25-0.3-2	122.7			162.83	1.33	186.38	1.52	121.59	0.99
16-10-50-0.2-1	126.0	0.58	1.35	161.42	1.28	182.83	1.45	125.64	1.00
16-10-50-0.2-2	126.6			161.42	1.28	182.83	1.44	125.64	0.99
16-10-50-0.3-1	120.6	0.6	1.75	165.67	1.37	189.67	1.57	121.67	1.01
16-10-50-0.3-2	121.4			165.67	1.36	189.67	1.56	121.67	1.00
16-15-50-0.2-1	136.8	0.55	1.15	170.67	1.25	190.27	1.39	135.84	0.99
16-15-50-0.2-2	138.4			170.67	1.23	190.27	1.37	135.84	0.98
16-15-50-0.3-1	132.0	0.56	1.40	179.70	1.36	201.8	1.53	135.20	1.02
16-15-50-0.3-2	134.5			179.70	1.34	201.8	1.50	135.20	1.01
19 mm-1	120.4	0.59	1.28	157.68	1.31	172.14	1.43	120.68	1.00
19 mm-2	120.2			157.68	1.31	172.14	1.43	120.68	1.00
19-10-50-0.2-1	155.1	0.6	1.10	189.19	1.22	206.4	1.33	154.95	1.00
19-10-50-0.2-2	155.9			189.19	1.21	206.4	1.32	154.95	0.99
19-10-50-0.3-1	152.1	0.62	1.30	196.63	1.29	216.93	1.43	154.22	1.01
19-10-50-0.3-2	155.9			196.63	1.26	216.93	1.39	154.22	0.99
19-15-50-0.2-1	173.6	0.65	1.15	206.22	1.19	228.98	1.32	174.65	1.01
19-15-50-0.2-2	176.6			206.22	1.17	228.98	1.30	174.65	0.99
				Mean	1.32		1.47		1.00
				CoV	0.078		0.077		0.012

5. Prediction of ultimate load

The ability of the dowel connection in transferring shear force, namely dowel action, could be investigated by analysing the deformation of the embedded dowel connection and the surrounding concrete. Rasmussen [57] assumed that the ultimate limit state (ULS) of the dowel connection embedded into concrete was the simultaneous occurrences of the localised concrete crushing at the joint surface and the plastic hinge formed in the dowel connection. This assumption had been verified through experimental tests conducted by Vintzēleou et al. [58] and Soroushian et al. [55]. To analyse these two typical failures and determine the ultimate load, a series of design equations had been proposed by researchers and validated against experimental test results [55, 57-66]. Rasmussen [57] recommended two empirical equations with and without considering the joint width as expressed by Eqs. (15) to (17), where the constant k_0 is determined according to experimental tests and equal to 1.3; z and d are the joint width and diameter of the dowel bar, respectively; f_y is the yield strength of the dowel connection.

$$V_{\mathrm{F,max}} = k_0 d^2 \sqrt{f_{\mathrm{c}} f_{\mathrm{y}}} \tag{15}$$

$$V_{\mathrm{F,max}} = k_0 \left[\sqrt{1+(\varepsilon k_0)^2} - (\varepsilon k_0) \right] d^2 \sqrt{f_{\mathrm{c}} f_{\mathrm{y}}} \tag{16}$$

$$\varepsilon = 3 \frac{z}{d} \sqrt{\frac{f_{\mathrm{c}}}{f_{\mathrm{y}}}} \tag{17}$$

Similar to the equations proposed by Rasmussen [57], Vintzēleou et al. [58] also proposed expressions for evaluating the dowel action. The strength improvement factor β_c equal to 5 had been incorporated to assess the maximum confined concrete compressive strength f_{c}^{*} within the localised crushing zone as expressed by Eq. (18). After considering the force and moment equilibriums, Eqs. (20) to (21) were derived to compute the maximum force transferred by an individual dowel connection, where $M_{\max}$ and $V_{\mathrm{F,max}}$ are the maximum moment at the plastic hinge and the maximum shear force carried by the dowel connection; l_0 is the distance between the plastic hinge and the joint surface. When the pavement joint width was equal to zero, the solution to Eq. (21) was equal to Eq. (15) proposed by Rasmussen [57].

$$f_{\mathrm{c}}^{*} = \beta_{\mathrm{c}} f_{\mathrm{c}} = 5 f_{\mathrm{c}} \tag{18}$$

$$M_{\max} = V_{\mathrm{F,max}} (z + 0.5 l_0) \tag{19}$$

$$f_{\mathrm{c}}^{*} d l_0 = V_{\mathrm{F,max}} \tag{20}$$

$$V_{\mathrm{F,max}}^2 + \left(10 f_{\mathrm{c}} z d\right) V_{\mathrm{F,max}} - 1\cdot 7 d^4 f_{\mathrm{c}} f_{\mathrm{y}} = 0 \tag{21}$$

Zhao et al. [63] also developed theoretical design equations to analyse the dowel action and considered the joint width z between concrete blocks, in which the strength improvement factor

β_c was equal to $\sqrt{3}$. Since varying stress improvement factors have been considered in the theoretical analysis, the proper range of β_c needs to be carefully determined. As suggested by Randl [60, 61], the confined concrete compressive strength should be 3 to 4 times the cube compressive strength. Rasmussen [57] recommended a stress improvement factor of 3 to 5 after considering the confinement effect. Because there was no uniform solution to the stress improvement factor, it was reasonable to determine β_c by fitting the theoretical analysis result to test data. Following the test setup, the force diagram of dowel connections embedded into concrete is shown in Fig. 24. Under the ultimate limit state (ULS), at the location of the plastic hinge, the maximum shear force transferred by the dowel connection $V_{F,max}$ was equal to the supporting force offered by the concrete as indicated in Eq. (22). For the moment equilibrium, as expressed by Eqs. (23) and (24), the moment at the plastic hinge was equal to the plastic moment resistance of the dowel connection M_{pl}. Therefore, the maximum dowel shear force at the joint surface $V_{F,max}$ was determined by Eqs. (25) to (27).

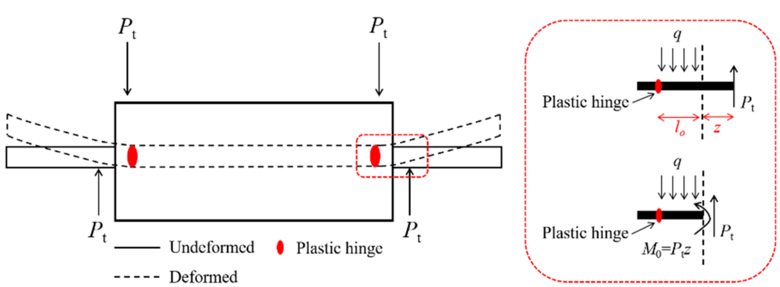

Fig. 24. The force diagram of dowel connections embedded in concrete.

$$V_{\mathrm{F,max}} = P_{\mathrm{t}} = q l_0 = d \beta_{\mathrm{c}} f_{\mathrm{c}} l_0 \tag{22}$$

$$M_{\mathrm{pl}} = \frac{f_{\mathrm{y(0.2)}} d^3}{6} \tag{23}$$

$$M_{\mathrm{pl}} = V_{\mathrm{F,max}} z + V_{\mathrm{F,max}}^2 / (2 \beta_{\mathrm{c}} f_{\mathrm{c}} d) \tag{24}$$

$$V_{\mathrm{F,max}} = k_{\mathrm{v}} A_{\mathrm{s}} \sqrt{f_{\mathrm{y(0.2)}} f_{\mathrm{c}}} \tag{25}$$

$$k_{\mathrm{v}} = \frac{4}{\pi}\left(\sqrt{\beta_{\mathrm{c}}^2 \alpha^2 + \frac{1}{3}\beta_{\mathrm{c}}} - \beta_{\mathrm{c}}\alpha\right) \tag{26}$$

$$\alpha = \frac{z}{d}\sqrt{\frac{f_{\mathrm{c}}}{f_{\mathrm{y(0.2)}}}} \tag{27}$$

After fitting the ultimate loads computed by Eq. (25) to test results, the stress improvement factors β_{c} were equal to 4.3 and 3.1 for specimens with 16 mm and 19 mm dowel connections, respectively. Due to a smaller contact area, it was reasonable that more severe compressive stress concentration was induced in specimens with 16 mm dowel connections, thereby resulting in a larger stress improvement factor.

In terms of the strength enhancement provided by the ring concrete, from Eq. (25), the maximum shear force $V_{\mathrm{F,max}}$ was closely related to the square root of the concrete compressive strength. The contact area between the ring part and the NSC concrete block also had a significant impact on the localised concrete crushing at the joint surface. As a result, a non-dimensional parameter $\sqrt{\frac{f_{\mathrm{c,ring}}}{f_{\mathrm{c}}}}\frac{t}{d}$ was proposed and analysed against the ultimate load ratio $N_{\mathrm{u,ring}}/N_{\mathrm{u,d}}$ calculated based on the experimental test results, where, $f_{\mathrm{c,ring}}$ is the cylinder compressive strength of the ring concrete; t refers to the ring thickness; $N_{\mathrm{u,ring}}$ and $N_{\mathrm{u,d}}$ represent the ultimate loads of the specimen strengthened by high-strength rings and that only with dowel connections, respectively. As displayed in Fig. 25, with a high coefficient of determination (R^2), a close linear relationship was observed between the ultimate load ratio and the non-dimensional parameter $\sqrt{\frac{f_{\mathrm{c,ring}}}{f_{\mathrm{c}}}}\frac{t}{d}$. Therefore, Eq. (28) was proposed to predict the ultimate load of the high-strength ring strengthened dowel connection. After being validated against test results, this equation was proved to be accurate in the ultimate load prediction as summarised in Table 9 and Table 10 and depicted in Fig. 26.

$$\frac{N_{\mathrm{u,ring}}}{N_{\mathrm{u,d}}}=0.281\sqrt{\frac{f_{\mathrm{c,ring}}}{f_{\mathrm{c}}}}\left(\frac{t}{d}\right)+1 \tag{28}$$

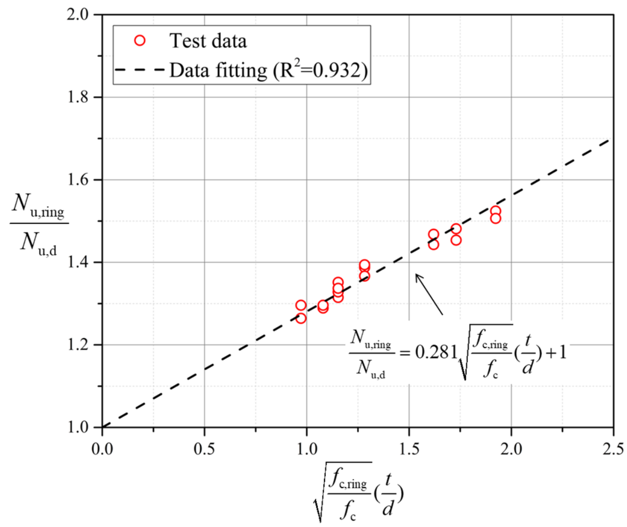

Fig. 25. Ultimate load prediction.

Table 9 Ultimate load obtained by test and predictions (16 mm).

Specimen ID	$N_{\mathrm{u,Test}}$	$\frac{t}{d}$	$\sqrt{\frac{f_{\mathrm{c,ring}}}{f_{\mathrm{c}}}}$	$\frac{t}{d}\sqrt{\frac{f_{\mathrm{c,ring}}}{f_{\mathrm{c}}}}$	$N_{\mathrm{u,Pred}}$	$N_{\mathrm{u,Pred}}/N_{\mathrm{u,Test}}$
16-1	89.9	-	-	-	-	-
16-2	91.6	-	-	-	-	-
16-10-25-0.2-1	126.3	0.63	2.05	1.28	123.52	0.98
16-10-25-0.2-2	124.1	0.63	2.05	1.28	123.52	1.00
16-10-25-0.3-1	119.4	0.63	1.85	1.15	120.96	1.01
16-10-25-0.3-2	122.7	0.63	1.85	1.15	120.96	0.99
16-10-50-0.2-1	126	0.63	2.05	1.28	123.52	0.98
16-10-50-0.2-2	126.6	0.63	2.05	1.28	123.52	0.98
16-10-50-0.3-1	121.4	0.63	1.85	1.15	120.96	1.00
16-10-50-0.3-2	120.6	0.63	1.85	1.15	120.96	1.00
16-15-50-0.2-1	136.8	0.94	2.05	1.92	139.87	1.02
16-15-50-0.2-2	138.4	0.94	2.05	1.92	139.87	1.01
16-15-50-0.3-1	132	0.94	1.85	1.73	136.04	1.03
16-15-50-0.3-2	134.5	0.94	1.85	1.73	136.04	1.01
					Mean	1.00
					CoV	0.017

Table 10 Ultimate load obtained by test and predictions (19 mm).

Specimen ID	$N_{\mathrm{u,Test}}$	$\frac{t}{d}$	$\sqrt{\frac{f_{\mathrm{c,ring}}}{f_{\mathrm{c}}}}$	$\frac{t}{d}\sqrt{\frac{f_{\mathrm{c,ring}}}{f_{\mathrm{c}}}}$	$N_{\mathrm{u,Pred}}$	$N_{\mathrm{u,Pred}}/N_{\mathrm{u,Test}}$
19-1	120.4	-	-	-	-	-
19-2	120.2	-	-	-	-	-
19-10-50-0.2-1	155.1	0.53	2.05	1.08	156.80	1.01
19-10-50-0.2-2	155.9	0.53	2.05	1.08	156.80	1.01
19-10-50-0.3-1	152.1	0.53	1.85	0.97	153.95	1.01
19-10-50-0.3-2	155.9	0.53	1.85	0.97	153.95	0.99
19-15-50-0.2-1	173.6	0.79	2.05	1.62	175.05	1.01

19-15-50-0.2-2	176.6	0.79	2.05	1.62	175.05	0.99
					Mean	1.00
					CoV	0.010

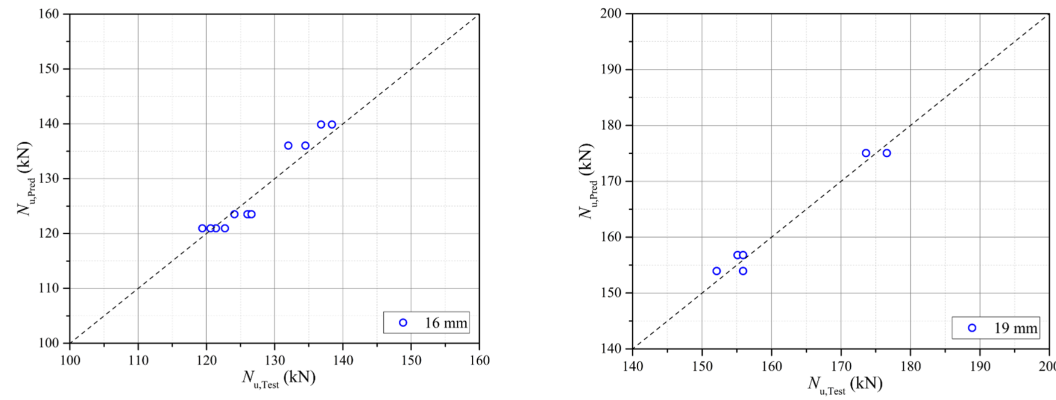

(a) (b)

Fig. 26. Ultimate load comparisons, (a) 16 mm dowel connections, (b) 19 mm dowel connections.

6. Conclusion

In this paper, an innovative high-strength ring strengthened dowel connection was proposed and experimentally investigated. Observed failure modes, deflection responses as well as the concrete strain development were reported and compared. Parameters including the compressive strength of the ring concrete, the high-strength ring thickness and length were studied in terms of the ultimate load and the initial stiffness enhancements and the mitigation of localised concrete crushing. Based on test observations, the following conclusions were drawn:

(1) After applying the high-strength rings, higher ultimate loads were achieved under vertical load due to the superior bearing resistance of the ring concrete.

(2) In contrast to the traditional dowel connections, the high-strength ring created a stiffer support for the embedded dowel connections, thereby improving the initial stiffness of the test specimen.

(3) Although the failure of the high-strength ring strengthened dowel connection was still governed by localised concrete crushing, the superior compressive behaviour of the ring

concrete delayed the initiation of the crushing zone around the dowel connection.

(4) With the expanded contact area between NSC and the ring concrete, the application of the ring part could effectively lower the compressive development of NSC and mitigate localised concrete crushing.

(5) Based on the deflection data obtained from experimental tests, the elastic and elasto-plastic deflection responses of the dowel connection embedded into concrete could be accurately predicted through BEF and BIF theories.

(6) With a non-dimensional parameter, an analytical solution was derived to predict the ultimate load of the high-strength ring strengthened dowel connection embedded into concrete.

To conclude, based on monotonic loading test results, the use of high-strength rings in dowel connections is a promising solution for improving the performance of these connections. However, as dowel connections are generally subject to millions of load repetitions within their service life, it is also crucial to evaluate the structural performance of the high-strength ring strengthened dowel connections from a fatigue perspective. Further tests and research will help to fully understand the durability and long-term performance of this connection system. Test results could serve as valuable references for designers and engineers to promote the design and the practical application of this high-strength ring strengthened dowel connection system.

Acknowledgements

The research work presented in this paper was supported by a grant from the Research Grants Council of the Hong Kong Special Administrative Region, China (Project no. R5007-18). The authors would like to sincerely thank the technical staff of the Structural Engineering Research

Laboratory and Concrete Technology laboratory for their support.